

The Secondary Spin Bias of Dark Matter Haloes

James W. Johnson,^{1,2*} Ariyeh H. Maller,^{3,4} Andreas A. Berlind,² Manodeep Sinha,^{2,6,7}
and J. Kelly Holley-Bockelmann^{2,5}

¹Department of Astronomy, The Ohio State University, 140 W. 18th Ave. Columbus, OH 43210, USA

²Department of Physics and Astronomy, Vanderbilt University, 2301 Vanderbilt Place, Nashville, TN 37235, USA

³Department of Physics, New York City College of Technology, CUNY, 300 Jay St., Brooklyn, NY 11201, USA

⁴Department of Astrophysics, American Museum of Natural History, New York, NY, USA

⁵Department of Physics, Fisk University, 1000 17th Ave. N, Nashville, TN 37208, USA

⁶Centre for Astrophysics and Supercomputing, Swinburne University of Technology, Hawthorn, Victoria 3122, Australia

⁷ARC Centre of Excellence for All Sky Astrophysics in 3 Dimensions (ASTRO 3D)

Accepted XXX; Received YYY; in original form ZZZ

ABSTRACT

We investigate the role of angular momentum in the clustering of dark matter haloes. We make use of data from two high-resolution N-body simulations spanning over four orders of magnitude in halo mass, from $10^{9.8}$ to $10^{14} h^{-1} M_{\odot}$. We explore the hypothesis that mass accretion in filamentary environments alters the angular momentum of a halo, thereby driving a correlation between the spin parameter λ and the strength of clustering. However, we do not find evidence that the distribution of matter on large scales is related to the spin of haloes. We find that a halo’s spin is correlated with its age, concentration, sphericity, and mass accretion rate. Removing these correlations strongly affects the strength of secondary spin bias at low halo masses. We also find that high spin haloes are slightly more likely to be found near another halo of comparable mass. These haloes that are found near a comparable mass neighbour - a *twin* - are strongly spatially biased. We demonstrate that this *twin bias*, along with the relationship between spin and mass accretion rates, statistically accounts for halo spin secondary bias.

Key words: cosmology: theory – large-scale structure of the universe – dark matter – galaxies: haloes

1 INTRODUCTION

High-resolution cosmological N-body simulations suggest that the spatial clustering of dark matter haloes is related to secondary properties other than halo mass (Sheth & Tormen 2004; Gao et al. 2005; Wechsler et al. 2006; Gao & White 2007; Wang et al. 2007; Li et al. 2008; Faltenbacher & White 2010; Lacerna & Padilla 2012; Lazeyras et al. 2017; Villarreal et al. 2017; Salcedo et al. 2018). These findings are notable because a simple spherical collapse model (Press & Schechter 1974) for halo formation predicts that spatial clustering should solely depend on halo mass (Mo & White 1996). This is a phenomenon dubbed *secondary bias* by Salcedo et al. (2018) because of the clustering dependance on halo properties in addition to halo mass. This has also been called *assembly bias* (Croton et al. 2007) in the past. However, high mass haloes do not exhibit a secondary bias with age, but do with concentration (Mao et al. 2018; Salcedo et al. 2018). Furthermore, Salcedo et al. (2018) showed that the secondary age and concentration biases can be accounted for by a correlation between these properties and the distance to a massive neighbour ($M_n \geq 10M_h$). This mechanism is

less related to the assembly histories of the haloes than it is a direct statement about the mass of the nearby neighbour. For this reason, we adopt the term secondary bias.

Secondary bias is of interest because it has the potential to shed light on the physical mechanisms by which dark matter haloes collapse and evolve. It is also of interest because of the many statistical models connecting galaxy clustering statistics to that of their host dark matter haloes, such as the halo occupation distribution (e.g. Peacock & Smith 2000; Scoccimarro et al. 2001; Berlind & Weinberg 2002; Cooray & Sheth 2002; Berlind et al. 2003; Zu & Mandelbaum 2015, 2016), the conditional luminosity function (e.g. Yang et al. 2003; van den Bosch et al. 2003), and subhalo abundance matching (e.g. Vale & Ostriker 2004; Conroy et al. 2006). These methods have usually operated under the assumption that the clustering of dark matter haloes is dependent only on mass, or a single parameter related to the mass¹. It may be tempting to assume that galaxies would inherit a secondary bias from the property-dependent clustering of their host haloes. Models where galaxy

* Contact e-mail: johnson.7419@osu.edu

¹ Note however that abundance matching models do account for any clustering bias from substructure by design.

color is determined by halo age (Hearin & Watson 2013) have been successfully used to explain the color dependence of galaxy clustering (Hearin et al. 2014, 2015). So far unexplored is the suggested connection between galaxy formation physics and halo spin (Fall & Efstathiou 1980; Mo et al. 1998; Somerville et al. 2008), although there are those who argue against such a connection (Maller & Dekel 2002; Brook et al. 2011, 2012; Somerville et al. 2018). If halo spin affects galaxy formation physics, then halo spin secondary bias would impact the galaxy-dark matter connection. Conversely, secondary spin bias would allow one to test whether galaxy formation models where galaxy size depends on halo spin are consistent with observational data.

The first studies to quantify halo secondary bias found that the clustering strength at fixed halo mass depends on the value of a wide range of secondary halo properties, from age to environment. In particular, haloes that are older (Sheth & Tormen 2004; Gao et al. 2005; Wechsler et al. 2006; Gao & White 2007; Wang et al. 2007; Li et al. 2008), more tightly concentrated (Wechsler et al. 2006; Gao & White 2007; Faltenbacher & White 2010; Lazeyras et al. 2017; Villarreal et al. 2017), spherically shaped (Faltenbacher & White 2010), have more substructure (Wechsler et al. 2006; Gao & White 2007), or high spin (Gao & White 2007; Faltenbacher & White 2010; Lacerna & Padilla 2012; Lazeyras et al. 2017; Villarreal et al. 2017) exhibit stronger clustering than their counterparts of similar mass. All of these biases, with the exception of spin, grow stronger for lower mass haloes. Recently, Lazeyras et al. (2017) showed that the mass accretion rates of haloes exhibit a similar phenomenon, with slowly accreting haloes exhibiting stronger clustering than their more quickly accreting counterparts. This bias is also strongest at low halo masses. In the case of spin, however, the bias is strongest at high masses.

Early interpretations placed the root cause of this bias on differences in the assembly histories of haloes; hence the term *assembly bias* from Croton et al. (2007). This was an attractive interpretation not only for its simplicity, but also because it would explain why the biases from halo properties related to the assembly histories of the haloes (e.g. concentration, shape, and amount of substructure) show a similar dependence on mass. However, some properties that are also directly related to the assembly history, such the time of the last major merger, do not exhibit assembly bias (Li et al. 2008; Salcedo et al. 2018). This suggests that assembly history may not be the only causal mechanism behind these clustering biases. Recently, Salcedo et al. (2018) showed that halo age and concentration are strongly correlated with the distance to a massive neighbour. That is, when one takes a subsample of old or highly concentrated haloes, they systematically select the ones that are closer in space to a much more massive system. This *neighbour bias* accounts for most of the secondary bias as a function of halo mass associated with halo age and concentration. Halo spin, however, showed only a weak dependence on the distance to a massive neighbour, and a correction for this relationship did not account for a significant portion of the associated signal. These results, along with the fact that the secondary bias from halo spin is seen to have the opposite dependence on halo mass, comprise the strong evidence that it has different causal mechanisms than the secondary biases from age and concentration.

Lacerna & Padilla (2012) suggested that in filaments, the preferred directionality of mass accretion could spin up the halo. Since filament haloes are in overdense regions, this could result in a correlation between halo spin and clustering statistics. In this paper, we test this hypothesis, as well as explore other possible explanations of halo spin secondary bias. We describe our simulations and the

methods we use to measure halo clustering in section 2. We provide an overview of secondary spin bias in section 3. We explore the correlation between halo spin and the anisotropy of the large scale matter distribution in section 4. In section 5, we detail correlations between spin and other halo properties. We demonstrate the role of *twin bias* in causing secondary spin bias in section 6. We end with discussion in section 7.

2 DATA AND METHODS

2.1 The Simulations

We use two high-resolution dark matter only simulations to study the secondary bias associated with halo spin. The first is named *Vishnu*, which has a box width of $130 h^{-1}$ Mpc and a particle mass of $3.215 \times 10^7 h^{-1} M_{\odot}$. Since the box size for *Vishnu* is relatively modest, the impact of cosmic variance can be large. To suppress the effects of cosmic variance, we needed to ensure that the modes close to the fundamental mode are not significantly different from linear theory. We generated 100 realizations of the initial conditions using 100 different random number seeds. The initial conditions with the smallest root-mean-square deviation from the linear theory power spectrum forms the basis for the *Vishnu* simulation. The second simulation is named *ConsueloHD*, which has a box width of $420 h^{-1}$ Mpc and a particle mass of $1.87 \times 10^9 h^{-1} M_{\odot}$. The initial power spectrum for both simulations was calculated using CAMB (Lewis & Challinor 2011). The initial positions and velocities of the particles at redshift $z = 99$ were then determined using the 2LPT code (Scoccimarro 1997). Both simulations evolved to $z = 0$ using the GADGET-2 N-body TreeSPH algorithm (Springel 2005) in a Λ CDM cosmology. Their sizes, particle masses, hubble parameters h , mass energy fractions Ω_M , dark energy fractions Ω_{Λ} , power spectrum normalizations n_s , and the mass density fluctuations at $8 h^{-1}$ Mpc σ_8 are presented in Table 1 along with the number of haloes. We use the ROCKSTAR and Consistent-Trees algorithms to find haloes (Behroozi et al. 2013a,b), adopting the virial definition of haloes with Δ_{vir} set by Bryan & Norman (1998). We set a minimum mass resolution of 200 gravitationally bound particles for each halo, corresponding to a virial mass of $10^{9.8} h^{-1} M_{\odot}$ and $10^{11.6} h^{-1} M_{\odot}$ for *Vishnu* and *ConsueloHD*, respectively. In this paper we only consider distinct haloes that do not live inside larger haloes (i.e. hosts or central haloes). We do not include subhaloes in the sample. We thus obtain a dataset of 706,060 and 707,880 haloes from *Vishnu* and *ConsueloHD*, respectively. By combining these two simulations, we obtain data spanning over four orders of magnitude in halo mass; from $10^{9.8}$ to $10^{14} h^{-1} M_{\odot}$.

In order to ensure that the differences in cosmology between *Vishnu* and *ConsueloHD* do not impact our measurements of halo spin secondary bias, we briefly employ data from the *Small Multi-Dark Planck* (SMDPL) simulation (Prada et al. 2012; Klypin et al. 2016). The cosmological parameters for this simulation are also summarized in Table 1 along with *Vishnu* and *ConsueloHD*. We again set a minimum mass resolution of 200 gravitationally bound particles ($M_h = 10^{10.3} h^{-1} M_{\odot}$) and remove all subhaloes. We thus obtain a dataset of 8,603,471 haloes from SMDPL. By using this simulation, we obtain data that spans the range in halo mass in which *Vishnu* and *ConsueloHD* overlap. Because SMDPL has cosmological parameters similar to *ConsueloHD* but different from *Vishnu*, this allows us to ensure that our measurements of halo spin secondary bias are independent of cosmology.

It has been shown that halo spin takes a large number of particles to converge in N-body simulations (Oñorbe et al. 2014; Benson

Table 1. A summary of the cosmological parameters for the simulations.

Name	Box Size [Mpc h^{-1}]	Particle Mass [$M_{\odot} h^{-1}$]	h	Ω_M	Ω_{Λ}	n	σ_8	N_{haloes}
Vishnu	130	3.215×10^7	0.70	0.25	0.75	1.0	0.8	706,060
ConsueloHD	420	1.87×10^9	0.681	0.302	0.698	0.96	0.828	707,880
SMDPL	400	9.63×10^7	0.678	0.307	0.693	0.98	0.8228	8,603,741

2017). With 200 particles, there are errors of order unity, and at least 4×10^4 particles are required for 10% precision. These errors will shuffle high and low spin haloes, **reducing** the secondary bias measured. In general, we consider just splitting the sample into two bins, and thus for low particle number haloes, one should interpret the measured spin biases as lower limits. For higher particle number haloes, this effect becomes negligible.

2.2 Halo Properties

We make use of each of the following halo properties in this analysis as measured using the ROCKSTAR and Consistent-Trees codes.

1. Halo Spin: We adopt a definition of halo spin according to a dimensionless parameter defined in Bullock et al. (2001):

$$\lambda \equiv \frac{J}{\sqrt{2}MVR} \quad (1)$$

where J is the total angular momentum of the halo, M is its virial mass, and V and R are the virial circular velocity and virial radius, respectively. We note that the original and an alternative definition of halo spin is defined in Peebles (1969) as:

$$\lambda_P \equiv \frac{J\sqrt{|E|}}{GM^{5/2}} \quad (2)$$

where E is the total energy of the halo (a negative value if it is bound) and G is Newton's gravitational constant. In this paper, we present results using the Bullock et al. (2001) definition, but we note that we have repeated our analysis with the Peebles (1969) definition, λ_P , and found qualitatively similar results.

2. Age: To measure age, we use the redshift at which a halo accumulated half of its present-day mass. This quantity is hereafter referred to as the *half mass redshift*, or $z_{1/2}$. This definition dictates that haloes which have lost mass will tend to be old, because half of their present day mass is less than half of their peak mass.

3. Concentration: To measure the halo concentration, we use the method introduced in Klypin et al. (2011). In this method, the maximum circular velocity is measured for each halo, and this is used to infer the halo's concentration under the assumption that it has an NFW density profile (Navarro et al. 1997). This has been shown to give the same value as the traditional definition of concentration $c_{\text{vir}} = R_{\text{vir}}/r_s$ when the density profile is well fit by the NFW profile. However, it provides much more reasonable values when the density profile deviates significantly from NFW.

4. Shape: We measure halo shape using the eigenvalues of the moment of inertia tensor applied to the particles within the halo as determined by ROCKSTAR (see Behroozi et al. (2013a) or section 4 for details). We use the square root of the ratio of the smallest to largest eigenvalues of this tensor as an indicator of the sphericity of the halo, where $(c/a)_{\text{halo}} = 1$ corresponds to a spherically symmetric distribution of matter.² This quantity does not contain information

about whether the halo itself is oblate or prolate. In fact, Schneider et al. (2012) showed that the more detailed shapes of haloes is a distribution which varies with virial mass. We thus employ this measure as a general diagnostic for ellipticity.

5. Accretion Rate: To measure halo mass accretion rates, we use the total mass accreted over the previous dynamical time of each halo. This value is determined by Consistent-Trees, and is denoted here by $\langle \dot{M} \rangle$, where the brackets denote that it is an average over the previous dynamical time. Since the accretion rate strongly depends on halo mass we use a relative accretion $\langle \dot{M} \rangle / \langle \dot{M} \rangle_{\text{max}}$ where $\langle \dot{M} \rangle_{\text{max}}$ is the maximum accretion rate of a halo in a given mass bin. This dimensionless parameter is then mass independent and can be used to compare the relative accretion rates of haloes across a range of halo masses.

6. Redshift of Last Major Merger: The most recent redshift where the halo had a merger with a mass ratio of at least 1:3 is denoted as z_{lmm} . Haloes that never have a merger of this ratio are given a value of z_{lmm} when they first have enough particles to be counted as a halo.

2.3 Statistical Measures

As a measure of halo clustering, we make use of the two-point autocorrelation function:

$$\xi(r) = \frac{DD(r)}{RR(r)} - 1 \quad (3)$$

where $DD(r)$ denotes the number of pairs of points separated within a scale range r and $r+dr$ within a given subsample of data, and $RR(r)$ is the number of pairs we would expect if the points were distributed randomly. We note that this formulation of ξ is generally noisier than that of Landy & Szalay (1993). However, in this analysis, we take advantage of the simple geometry of a simulation box to calculate $RR(r)$ analytically, and therefore with no associated error:

$$RR(r) = \frac{1}{2} \frac{N^2}{L^3} \frac{4}{3} \pi \left[(r+dr)^3 - r^3 \right] \quad (4)$$

where N denotes the number of haloes in the sample, and L is the width of the box. By implementing the two-point autocorrelation in this manner, the only source of noise in our measurements is in $DD(r)$. Because of the large number of haloes in our box the associated error is small. We calculate these errors using the jackknife method. Haloes are split into eight subsamples corresponding to each of the eight octants of the box. $\xi(r)$ is then calculated 8 times, each with one octant removed from the data. The associated error in ξ is then given by the jackknife formula with 8 subsamples:

$$\sigma_{\xi}(r) = \sqrt{\frac{7}{8} \sum_{i=1}^8 (\xi_i(r) - \langle \xi(r) \rangle)^2} \quad (5)$$

As a measure of the secondary bias associated with some secondary property of a halo S , we retain the following definition from Salcedo et al. (2018):

$$b_S^2(r|M_h, S) = \frac{\xi_{hh}(r|M_h, S)}{\xi_{hh}(r|M_h)} \quad (6)$$

² We include the subscript on $(c/a)_{\text{halo}}$ because we employ a similar notation in quantifying the anisotropy of the large scale matter distribution.

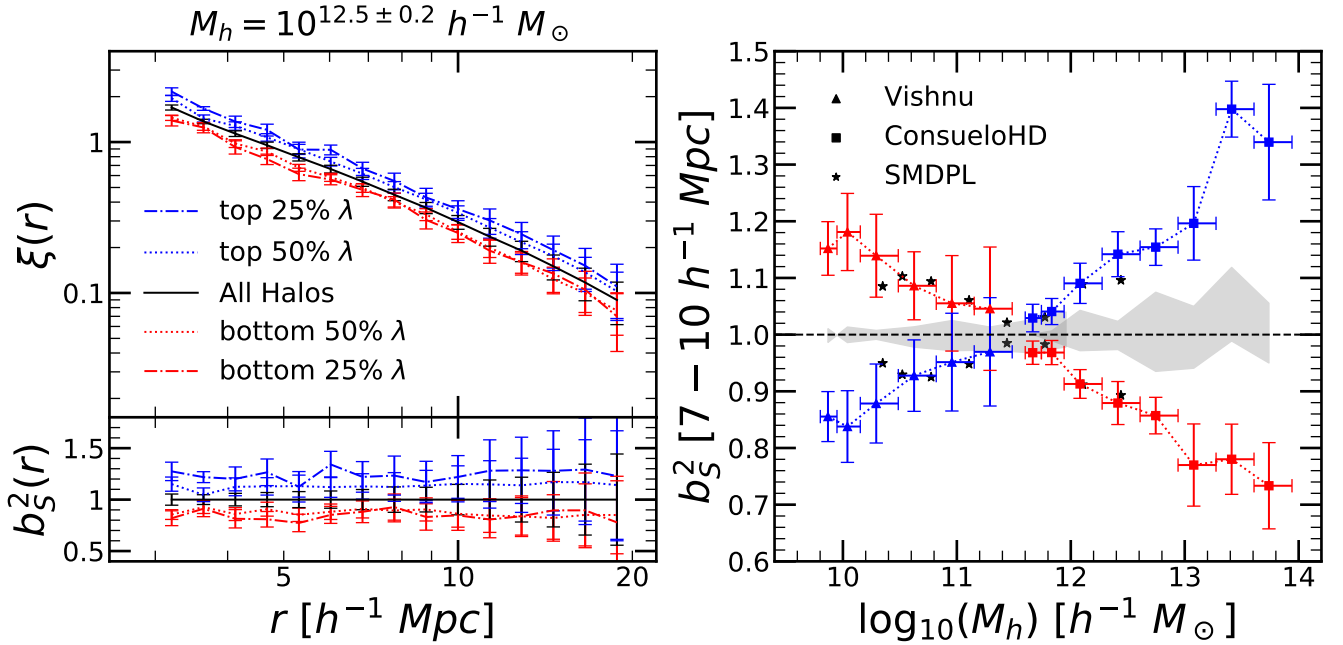


Figure 1. *Top-Left:* The two-point autocorrelation as a function of scale range using only ConsueloHD haloes with virial masses between $10^{12.3}$ and $10^{12.7} h^{-1} M_\odot$. We show the autocorrelation of the entire mass range in the black solid line, and low and high spin samples in red and blue, respectively. *Bottom-Left:* The ratio of the autocorrelations of each subsample and the entire mass bin. This is the relative bias for these subsamples as a function of scale range. *Right:* The relative bias as a function of halo mass measured between 7 and $10 h^{-1}$ Mpc for the 50% highest and lowest spinning haloes in each mass bin. The black dashed line corresponds to $b_S^2 = 1$, corresponding to the absence of a secondary bias by definition. The shaded region shows the finite bin width error, which is obtained by splitting bins in halo mass by the halo mass itself and measuring the relative bias. Triangles and squares denote measurements made with Vishnu and ConsueloHD haloes, respectively. We overplot in black stars the same measurements from the SMDPL simulation. The good agreement between Vishnu and SMDPL demonstrates that the small differences in cosmological parameters between these two simulations do not significantly impact secondary bias.

where $\xi_{hh}(r|M_h)$ denotes the autocorrelation of the haloes conditioned on some mass bin M_h . $\xi_{hh}(r|M_h, S)$ is precisely that, but also conditioned on some halo secondary property S (e.g. age, concentration, or spin). Under this formulation, $b_S^2 = 1$ for all haloes within a given mass range by design. **We emphasize that this is not the traditional definition of bias, which is relative to the underlying dark matter distribution.** This is a relative bias of a subsample against a halo mass bin which itself is biased compared to the dark matter density distribution.

We also use the jackknife method in determining errors in b_S^2 . We again use the octants of the box as subsamples, and obtain errors in a manner analogous to that of equation 5. That is, the autocorrelation and bias are separately calculated for each subsample with one octant removed. The variance is then calculated off of these eight measurements. However, the values for ξ and b_S^2 that we report, are those which are obtained from all of the haloes.

3 HALO SPIN SECONDARY BIAS

We begin by measuring the scale and mass dependence of halo spin secondary bias via the statistical measures outlined in section 2.3. The top-left panel of Figure 1 shows the two-point autocorrelation function for only ConsueloHD haloes with masses between $10^{12.3}$ and $10^{12.7} h^{-1} M_\odot$ for various subsamples in λ . Red and blue lines denote low versus high λ subsamples, respectively, with dotted and dot-dashed lines differentiating between halves and quartiles. We

show this in comparison to what is obtained when we take into account the entire mass range, shown by the solid black line. This is the essence of halo spin secondary bias. In a sample of haloes that have roughly the same mass, those that have higher values of λ exhibit stronger clustering than what would be expected from their mass alone. In turn, those that are of lower λ exhibit weaker clustering.

The bottom-left panel of Figure 1 shows the ratios that are obtained when we divide the autocorrelations of the spin subsamples by that of the entire mass range. The color and line-style scheme is the same as described above. This ratio is the secondary bias, b_S^2 . The secondary bias associated with λ is relatively scale independent, consistent with a straight line within the errors. For the rest of this paper we will focus on the clustering in the range between 7 and 10 Mpc h^{-1} . Because of this scale independence, this decision is arbitrary and should not impact our results. We have verified that this is indeed the case.

While the secondary bias of other halo properties like age and concentration has been shown to be driven by the $\sim 10\%$ extremes of the distribution, this is not the case for spin (Salcedo et al. 2018). We have verified this result as well. The relatively linear increase in b_S^2 between the half and quartile subsamples in λ also illustrates this. Because the increase in bias when using quartiles is rather modest, throughout this paper we split mass bins into halves in order to have more haloes in each bin.

The right-hand panel of Figure 1 shows the secondary bias at this length scale for a wide range of halo masses and simulations.

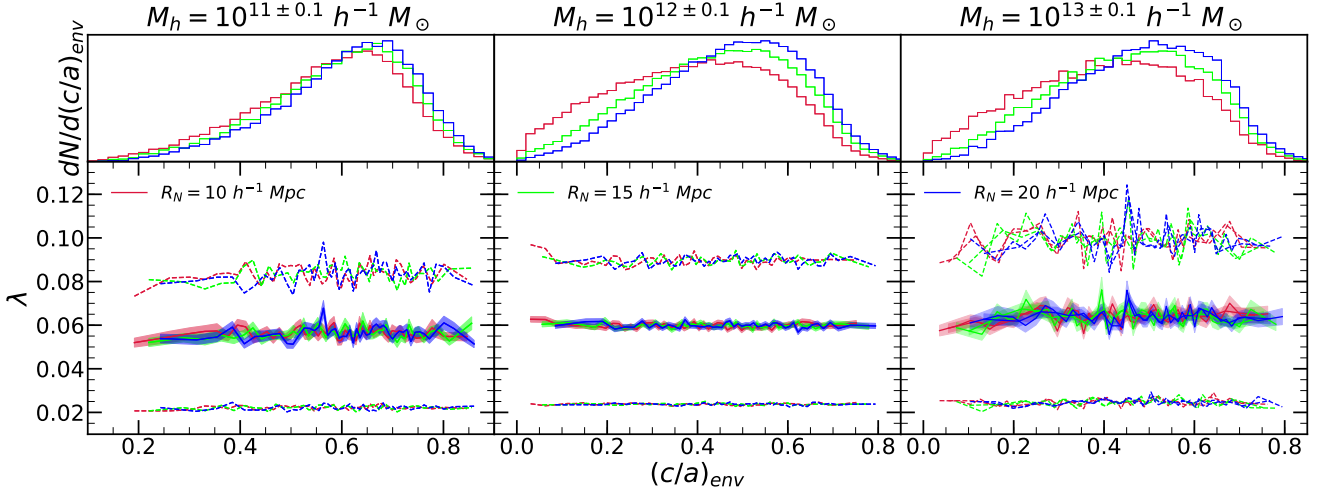


Figure 2. Measurements of the local anisotropy (i.e. non-sphericity) of the large-scale matter distribution as measured by the eigenvalues of the moment of inertia tensor applied to neighbouring haloes out to a distance R_N from a central halo. We plot the implied minor-to-major axis ratio $(c/a)_{\text{env}}$ from this tensor against the spin parameter λ for haloes with virial masses of $10^{11 \pm 0.1} h^{-1} M_\odot$ (left), $10^{12 \pm 0.1} h^{-1} M_\odot$ (middle), and $10^{13 \pm 0.1} h^{-1} M_\odot$ (right) for $R_N = 10$ (red), 15 (green), and 20 (blue) $h^{-1} \text{Mpc}$. Solid lines show the mean $(c/a)_{\text{env}}$ vs. λ in equal number bins. Shaded regions correspond to the uncertainty in the mean spin, and the dashed lines denote the range in λ containing 68.2% of the haloes in that bin, centered on the median. Our $(c/a)_{\text{env}}$ statistic is a proxy for filamentary structure, and the distributions of haloes in this quantity for each value of R_N are shown in the top panels. We use Vishnu haloes in the $10^{11 \pm 0.1} h^{-1} M_\odot$ sample, and ConsueloHD haloes in the remaining two.

We use triangles and squares to denote measurements made with Vishnu and ConsueloHD datasets, respectively. We also include b_S^2 as calculated from the SMDPL simulation (Prada et al. 2012; Klypin et al. 2016). We plot these measurements as black stars for both high and low λ samples and omit the error bars for clarity. The shaded region denotes the relative bias that we measure when we split our bins in halo mass by the halo masses themselves, referred to as the *finite bin width error* (Salcedo et al. 2018). This region quantifies the maximum error due to the intrinsic width of the mass bins used in our analysis, and represents the relative bias that would be measured from any secondary property if it were perfectly correlated with halo mass.

As one can see, the measured relative bias is in excellent agreement across all three simulations. Since SMDPL has almost the same cosmological parameters to ConsueloHD, but different from Vishnu, we conclude that the relative spin bias is independent of cosmology, at least for the modest cosmology differences probed here. For the remainder of this paper we use Vishnu and ConsueloHD.

Here we see results similar to that obtained by previous studies of halo spin secondary bias (Gao & White 2007; Faltenbacher & White 2010; Lacerna & Padilla 2012; Salcedo et al. 2018). Halo spin exhibits the strongest secondary bias in the high mass regime, and this falls off in lower mass ranges. We also see that this trend continues, producing a turnover at $\sim 10^{11.5} h^{-1} M_\odot$, below which low λ haloes exhibit slightly stronger clustering. This was also found recently by Sato-Polito et al. (2018) using the SMDPL simulation. It appears that this feature has not been seen in previous studies of halo secondary bias because Sato-Polito et al. (2018) and ours are the first studies to use simulations with a high enough resolution to make measurements at sufficiently low halo masses.

We do note from Figure 1 that the relative bias decreases for the lowest mass bins in Vishnu and SMDPL. It is likely that these measurements are affected by the errors in spin associated with low particle number haloes (Oñorbe et al. 2014; Benson 2017), which will inevitably cause shuffling between high and low spin

samples. This suggests that these are systematic underestimates of the true relative bias in these mass ranges. These measurements should therefore be interpreted qualitatively as lower limits on the relative bias. We however note that this source of error has no obvious effect outside of the lowest mass bin.

4 LOCAL ANISOTROPY

We continue by testing the hypothesis raised by Lacerna & Padilla (2012) that halo spin secondary bias is driven by filamentary structure. They conjectured that dark matter accretes onto haloes with a preferred directionality in filaments. This could cause an increase in halo angular momenta, and thereby spin. Filamentary environments are more likely to be overdense and could therefore connect λ to clustering statistics. To study this, we measure the local anisotropy (i.e. non-sphericity, elongation) of the halo distribution of surrounding haloes in the following manner. For each halo above our resolution limit, we measure the moment of inertia tensor of the haloes in the local neighbourhood defined by a *neighbourhood radius*, denoted R_N . For a neighbourhood with N haloes having masses denoted by m_i at a separation of $d_i \leq R_N$ from the host, the moment of inertia tensor is given by:

$$I \equiv \sum_{i=1}^N m_i \begin{bmatrix} dy_i^2 + dz_i^2 & -dx_i dy_i & -dx_i dz_i \\ -dx_i dy_i & dx_i^2 + dz_i^2 & -dy_i dz_i \\ -dx_i dz_i & -dy_i dz_i & dx_i^2 + dy_i^2 \end{bmatrix} \quad (7)$$

This tensor has three positive definite eigenvalues. We denote the square root of the ratio of the smallest to largest eigenvalue as $(c/a)_{\text{env}}$, analogous to the axis ratios for haloes as discussed in section 2.2.

In Figure 2, we present results comparing halo spin to $(c/a)_{\text{env}}$ in three different mass ranges ($M_h \approx 10^{11}$ (red), 10^{12} (green), and $10^{13} h^{-1} M_\odot$ (blue)) and for three different neighbourhood radii ($R_N = 10$ (left), 15 (middle), and 20 $h^{-1} \text{Mpc}$ (right)). The lowest mass bin contains haloes only from Vishnu, while the other two use

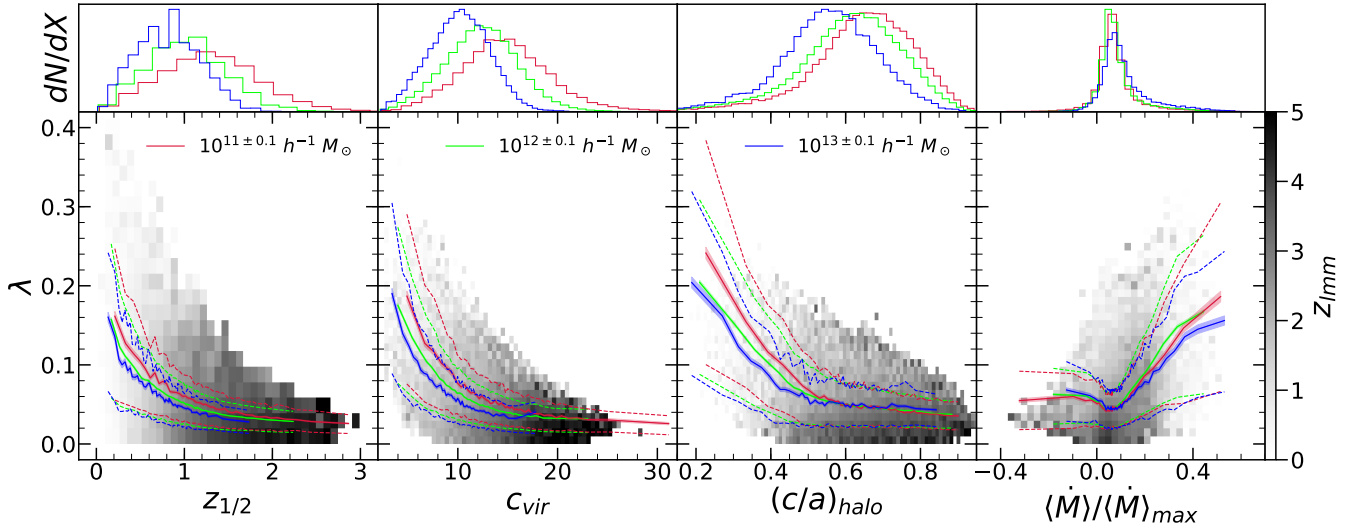


Figure 3. Halo spin λ as a function of $z_{1/2}$ (left), c_{vir} (left-middle), $(c/a)_{\text{halo}}$ (right-middle), and $\langle \dot{M} \rangle / \langle \dot{M} \rangle_{\text{max}}$ (right) for haloes with virial masses of $10^{11 \pm 0.1} h^{-1} M_{\odot}$ (red), $10^{12 \pm 0.1} h^{-1} M_{\odot}$ (green), and $10^{13 \pm 0.1} h^{-1} M_{\odot}$ (blue) $h^{-1} M_{\odot}$. Solid lines show the mean spin as a function of each parameter while the shaded regions show the error in that mean. Dashed lines denote the region of λ containing 68.2% of the haloes in each bin, centered on the median. Shown in grayscale is the mean redshift of the last major merger z_{lmm} within each pixel, where a merger event is counted if the mass ratio of the merging haloes is at least 1:3. Top panels show the probability distribution functions of haloes in each secondary property for each of the three mass ranges. The $10^{11 \pm 0.1} h^{-1} M_{\odot}$ sample contains haloes from Vishnu, while the remaining two contain haloes from ConsueloHD.

haloes from ConsueloHD. The upper panels show the normalized distributions of haloes in $(c/a)_{\text{env}}$. They clearly show that with increasing R_N , the distribution shifts gradually toward values closer to unity. This is as expected, since on larger scales we expect the matter distribution to become more isotropic until it eventually reaches a fully homogenous distribution.

The lower panels of Figure 2 show the mean λ in equal number bins in $(c/a)_{\text{env}}$ in each mass range and for each neighbourhood radius. Shaded regions denote the associated error in the mean λ , and dotted lines quantify the 68.2% dispersion in λ for each bin, centered on the median. There does not appear to be any significant correlation between halo spin and $(c/a)_{\text{env}}$ in any mass range or on any scale. That is, $(c/a)_{\text{env}}$ appears to uniformly sample the distribution of haloes in λ .

While we have only presented correlations between λ and $(c/a)_{\text{env}}$ here, we note that we have found similar results with $(b/a)_{\text{env}}$ and $(c/b)_{\text{env}}$. We also find that $(c/b)_{\text{env}} = 0.9 \pm 0.1$ for nearly all haloes in both Vishnu and ConsueloHD. This suggests that a prolate spheroid is a reasonable description of the mass distribution. Our $(c/a)_{\text{env}}$ variable is thus a proxy for filamentary structure.

It appears that λ is not statistically sensitive to filamentary structure. This would suggest that filamentary environments do not produce systematically high spin haloes, and without this correlation, they cannot be the physical explanation for its associated secondary bias. Whether or not $(c/a)_{\text{env}}$ shows its own secondary bias would be irrelevant, because these environments would uniformly sample the spin distribution.

5 AGE, CONCENTRATION, SPHERICITY, AND MASS ACCRETION

Finding that the anisotropy of the large scale halo distribution is not correlated with halo spin and therefore not likely to be responsible for its associated secondary bias, we turn to examining the

correlation between spin and other halo properties in search of an explanation for this phenomenon. In this section we present results showing correlations between halo spin and halo age, halo concentration, halo sphericity, and the rate of mass accretion onto the halo as we have defined them in Section 2.2. Figure 3 shows these relationships for the $10^{11 \pm 0.1}$, $10^{12 \pm 0.1}$, and $10^{13 \pm 0.1} h^{-1} M_{\odot}$ mass ranges in red, green, and blue, respectively. As in Figure 2, we plot the mean λ in equal number bins in each secondary property, with shaded regions denoting the error in the mean and dashed lines quantifying the 68.2% variance centered on the median in each bin. In the right-hand panel, we show the normalized mass accretion rate where the accretion rate is divided by the maximum rate in that mass bin. The one object with a value of unity in this quantity is off the plot as all other values, by construction, are less than this.

In the top panels, we show the normalized distributions of haloes in each of these secondary properties. These distributions illustrate known trends of these secondary properties with halo mass. Higher mass haloes tend to be younger, less concentrated, and more ellipsoidal than those of lower mass. When the mass accretion rates of haloes are normalized in this manner, however, it appears to be rather uniform across mass ranges. We note that there are strong inverse relationships between λ and each of $z_{1/2}$, c_{vir} , and $(c/a)_{\text{halo}}$. Thus high λ haloes tend to be younger, less concentrated, and more aspherical than other haloes. We also note a strong direct relationship between λ and $\langle \dot{M} \rangle$; high λ haloes tend to also be accreting mass at a faster rate.

To understand why these correlations exist, we overplot in gray scale the mean redshift at which haloes in the mass range $10^{12 \pm 0.1} h^{-1} M_{\odot}$ have had a major merger (mass ratio greater than 1:3). Clearly high spin haloes are more likely to have had recent major mergers, which is not surprising because in a major merger the orbital angular momentum of the haloes is converted to spin angular momentum (Vitvitska et al. 2002; Maller et al. 2002; Drakos et al. 2018a,b). Furthermore, age, concentration, sphericity, and mass ac-

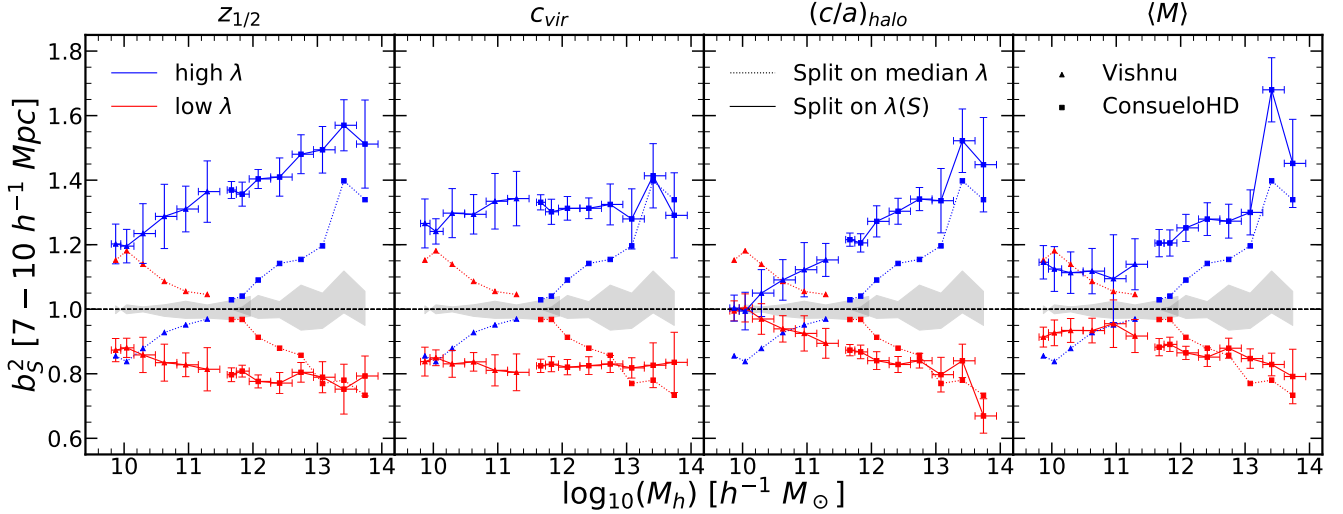


Figure 4. The relative bias as a function of halo mass for high (blue) and low (red) spin subsamples. Dotted lines show the relative bias that we measure when splitting mass bins into the 50% highest and lowest spinning haloes (these lines are identical to the dotted lines in the right panel of Fig. 1). Solid lines show the relative bias that we measure when we draw high and low spin samples while controlling for $z_{1/2}$ (left panel), c_{vir} (left-middle panel), $(c/a)_{\text{halo}}$ (right-middle panel), and $\langle \dot{M} \rangle$ (right panel). We do this by fitting a sixth-order polynomial to the median λ as a function of each property, and selecting haloes with spins above and below this curve. This is done within each individual bin in halo mass. Triangles and squares represent measurements made with Vishnu and ConsueloHD haloes, respectively. The shaded region denotes the finite bin width error, which we obtain by splitting bins in halo mass by the halo masses themselves and measuring the relative bias. The black dashed line highlights $b_S^2 = 1$.

cretion all also show correlation with the redshift of the last major merger. Younger haloes will tend to have lower z_{1mm} because our measurement of halo age $z_{1/2}$ is directly related to its mass assembly history. The relationship between z_{1mm} and c_{vir} is probably due to mergers; following a merger event, the core of the halo will require a finite amount of time to dynamically relax. This will increase the scale radius of the halo, thus decreasing the concentration. As new material accretes onto the halo, not through major mergers, it will add mass to the outer part of the halo, increasing the virial radius and thus increasing the concentration. Likewise a major merger will tend to enhance the density in the plane of the merger, making the halo's shape more ellipsoidal. Finally, after a major merger, it is not surprising to find a higher accretion rate. This is not only because major mergers are often associated with increased rates of accretion, but also because some material in the merger may take multiple orbits before being included in the virial mass.

We note that the grayscale in the λ - c_{vir} plane extends to $z_{\text{1mm}} \approx 5$. In the simulated cosmology, redshifts this high correspond to lookback times comparable to the Hubble time. This is much larger than the dynamical time of any physically realistic halo, indicating that the response to a merger event is not the only physical process influencing the spins of these haloes. This suggests that something related to a lack of major mergers is also influencing this correlation.

Each of the secondary properties plotted against spin in Figure 3 has an associated secondary bias. Specifically, the secondary bias associated with each of $z_{1/2}$, c_{vir} , $(c/a)_{\text{halo}}$, and $\langle \dot{M} \rangle$ is such that haloes that tend to be low λ exhibit stronger clustering than those that tend to be high λ in the low mass regime. This means that one would naively expect low spin haloes to exhibit stronger clustering, which is not true for haloes with masses $M_h \gtrsim 10^{11.5} h^{-1} M_\odot$. To decouple spin from these correlated properties, we adopt the following statistical correction. For each mass bin within which we measure b_S^2 , we first fit a sixth-order polynomial to the median

relationship between λ and one of these secondary properties S . We then draw high and low λ subsamples based off of the haloes that lie above or below the curve that we obtain. Thus the split is done for $\lambda(S)$, the spin as a function of another parameter, rather than the median lambda in each mass bin $\bar{\lambda}$. This procedure ensures that our high and low spin samples have identical distributions in S .

After drawing high and low λ samples in this manner for each of $z_{1/2}$, c_{vir} , $(c/a)_{\text{halo}}$, and $\langle \dot{M} \rangle$, we measure the relative bias as a function of halo mass, and plot our results in Figure 4. From left to right, the panels show the secondary bias associated with λ as a function of $z_{1/2}$, c_{vir} , $(c/a)_{\text{halo}}$, and $\langle \dot{M} \rangle$. Solid lines show the values of b_S^2 for spin split based on a function of another halo property $\lambda(S)$, while dotted lines show the relative bias when split by the median spin in each bin. The dotted lines here are the same as the dotted lines in Figure 1; for clarity, we have omitted their error bars. The clustering of high and low λ haloes is shown in blue and red, respectively. Because the adjusted subsamples are drawn from a polynomial fit, they do not necessarily split the subsamples evenly.

When splitting the samples based on spin as a function of another halo property, we see similar behavior across all four parameters studied here. Most notably, the turnover in the signal previously seen at $10^{11.5} h^{-1} M_\odot$ is no longer present. In all cases, the slope of the halo mass dependence of the secondary bias is reduced; for concentration, it becomes nearly flat. That is, we find that removing spin's correlation with age, concentration, halo shape, or mass accretion rate removes much of the halo mass dependence of b_S^2 , while still producing a secondary bias. Thus we see that in the low mass regime, secondary spin bias is closely intertwined with age, concentration, halo shape, and mass accretion rate. As these four properties are all correlated with one another, it is likely that we are seeing a single phenomenon responsible for most of the halo mass dependence for spin secondary bias. We note that at the high

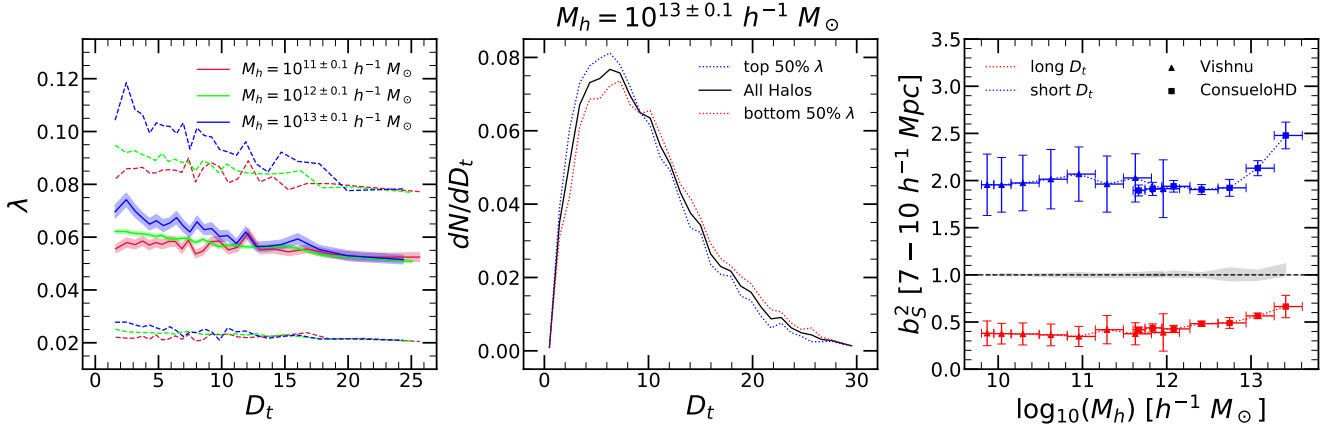


Figure 5. *Left:* Spin vs. twin distance for haloes with virial masses of $10^{11 \pm 0.1}$ (red), $10^{12 \pm 0.1}$ (green), and $10^{13 \pm 0.1}$ ($h^{-1} M_\odot$). Twin distance refers to the distance from a halo to a neighbouring halo between 1 and 3 times its own mass divided by the neighbour’s virial radius. We plot the mean halo spin in equal number bins of D_t , with shaded regions denoting the error in that mean. Dashed lines denote the range in λ containing 68.2% of haloes, centered on the median λ in that bin. The $10^{11 \pm 0.1} h^{-1} M_\odot$ sample contains haloes from Vishnu, while the remaining two contain haloes from ConsueloHD. *Middle:* Normalized distributions of D_t for the $10^{13 \pm 0.1} h^{-1} M_\odot$ sample from ConsueloHD. The black solid line shows the distribution for the entire mass range, while colored lines show that of the spin subsamples. *Right:* The relative bias as a function of halo mass for the 50% shortest (blue) and longest (red) D_t samples. Triangles and squares denote measurements made from Vishnu and ConsueloHD haloes, respectively. The black dashed line represents $b_S^2 = 1$. The shaded region shows the finite bin width error, which we obtain by splitting our bins in halo mass by the halo mass itself and measuring the relative bias.

mass end, the effect of splitting on spin as a function of another halo property is much smaller. In the next section, we explore an environmental halo property to explain this residual secondary bias.

6 TWIN BIAS

Based on the results of the previous section, it appears that none of the environmental or halo properties we have explored thus far can account for secondary spin bias. In this section, we therefore turn to studying a new environmental property: a halo’s distance to a neighbouring halo of comparable mass. Salcedo et al. (2018) showed that there was little correlation between spin and the distance to a ten or greater times as massive halo. Here we find that there is a correlation between spin and the distance to a halo of comparable mass, or a *twin* halo. We adopt the following unitless halo distance parameter from Salcedo et al. (2018):

$$D_t = \frac{D}{R_{\text{vir},t}} \quad (8)$$

where D denotes the halo-centric distance from the host to the neighbour of comparable mass, and $R_{\text{vir},t}$ is the **neighbour’s** virial radius. We have changed subscripts from D_n (adopted by Salcedo et al. 2018) to D_t to emphasize that this distance is to a twin in mass - not a much more massive neighbour. For every halo, we record the distance to the nearest twin, where the twin is required to be a halo of mass between 1 and 3 times the halo’s mass. We plot λ of haloes in three mass ranges against this quantity in the left-hand panel of Figure 5. Results are shown for haloes of virial masses $10^{11 \pm 0.1}$, $10^{12 \pm 0.1}$, and $10^{13 \pm 0.1} h^{-1} M_\odot$ in red, green, and blue, respectively. Shaded regions here denote the error in the mean λ in equal number bins, while dotted lines show the range in λ containing 68.2% of haloes, centered on the median value. The lowest mass bin contains haloes from Vishnu, while the other two bins are composed of haloes from ConsueloHD.

Figure 5 shows a rather weak, yet clear anticorrelation between λ and twin-distance which gets stronger with increasing halo mass.

This relationship does not flatten off, but appears to continue to large values of D_t . At high D_t , haloes in all mass ranges have a mean spin of $\lambda \approx 0.05$, but in the highest mass range, the lowest D_t haloes have a mean spin of $\lambda \approx 0.07$. Highly elongated or non-concentrated haloes, however, have a mean spin of $\lambda \approx 0.2$, a much more substantial effect.

In the middle panel, we show probability distribution functions in D_t for haloes in the $10^{13 \pm 0.1} h^{-1} M_\odot$ sample. The black line denotes the entire data in this mass range, while colored lines denote high and low samples in λ . These distributions clearly show a selection effect associated with λ , whereby subsamples of high λ haloes are systematically more likely to be found at low D_t - that is, fewer virial radii from a neighbour of comparable mass. In this same mass range, the high spin sample contains 22 and 14% more haloes at $D_t \leq 5$ and 10 than the low spin sample, respectively.

While the relationship between λ and D_t is subtle, the distance to a twin is a very spatially biased property, as can be seen in the right-hand panel of Figure 5. This panel shows a strong secondary bias of $b_S^2 \approx 2$ for low D_t haloes at lower masses, which then begins to increase near the redshift dependent collapse mass $M_* \approx 3 \times 10^{12} h^{-1} M_\odot$. Because the λ - D_t relation and the intrinsic spatial bias of twin haloes are both mass-dependent, it is likely that this influences the mass dependence of secondary spin bias for high mass haloes.

This bias is significantly stronger than the secondary spin bias, as well as the secondary biases from age, concentration, halo shape, and mass accretion. This is unsurprising, because low D_t haloes are by definition near a neighbour of comparable mass. Despite the subtlety of spin’s relationship with twin distance, it’s secondary bias may be significantly sensitive to D_t due to this strong spatial bias.

We test the sensitivity of halo spin secondary bias to this relationship by fitting a sixth-order polynomial under the same prescription as in section 5 to λ as a function of D_t . We assign haloes to be high or low λ based on whether or not they lie above or below this curve. We show our results in the bottom-right panel of Figure 6. In this figure, the dotted lines are the same as in Figure 1, the bias when λ is split by the median in each mass bin; we have again

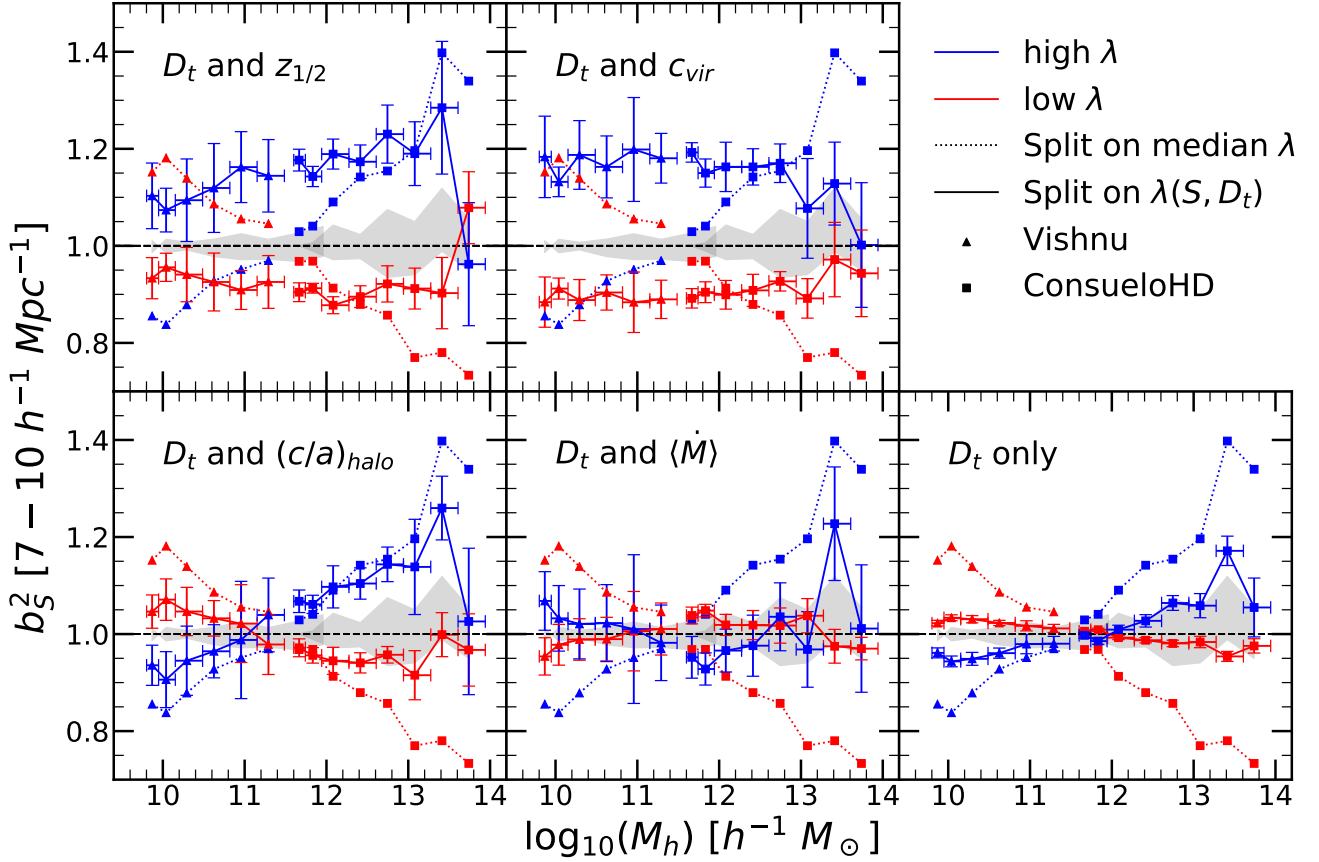


Figure 6. The relative bias as a function of halo mass. Dotted lines show that of the 50% highest and lowest spinning haloes in each mass bin (and are identical to the dotted lines in the right panel of Fig. 1). Solid lines show the relative bias for spin samples that are obtained while controlling for one or two secondary properties in each individual mass bin (i.e. such that both spin samples have statistically similar distributions in these properties). In the bottom-right panel, this is done for twin distance D_t only. This refers to the distance to a neighbouring halo between 1 and 3 times as massive as the halo itself divided by that neighbour’s virial radius. In the remaining panels, we jointly control for both D_t and each of $z_{1/2}$ (top-left), c_{vir} (top-middle), $(c/a)_{halo}$ (bottom-left), and $\langle \dot{M} \rangle$ (bottom-middle). The black dashed line represents $b_S^2 = 1$ everywhere, while the shaded region denotes the finite bin width error, which is obtained when we split our bins in halo mass by the mass itself and measure the relative bias.

omitted the error bars on these measurements for visual clarity. Solid lines show the relative bias that is measured when high and low λ subsamples in each mass bin are split by spin as a function of D_t , thus ensuring that they have identical D_t distributions. Under this prescription, the relative bias decreases significantly in all mass ranges. Above the turnover at $10^{11.5} h^{-1} M_\odot$, the signal that remains is largely consistent with the finite bin width error to within 1σ , with an outlier in one mass bin. Below the turnover, while its strength diminishes substantially, a small relative bias remains. It would thus appear that the subtle relationship between λ and D_t is enough to statistically account for a large portion of the signal associated with secondary spin bias.

For the other panels in Figure 6, we determine spin as a function of both twin distance and a second halo property. In each mass bin, we fit a 2-dimensional polynomial surface to λ as a function of both D_t and another secondary property. The function fit is simply the sum of two sixth-order polynomials: one a function of D_t and the other a function of $z_{1/2}$, c_{vir} , $(c/a)_{halo}$ or $\langle \dot{M} \rangle$. We then assign haloes to be high or low spin based on the fitted spin value, $\lambda(D_t, S)$. In other words, we control for both D_t and one of these secondary properties simultaneously.

The top-left and top-middle panels show b_S^2 as a function of the log of the halo mass in $h^{-1} M_\odot$ when we correct our high and low λ subsamples for D_t in combination with $z_{1/2}$ and c_{vir} , respectively. The secondary bias in these panels is now close to mass independent. That is, the combination of spin’s dependence on twin distance and either age or concentration seems to account for the mass dependence that we see in spin secondary bias when split on the median in each mass bin. For the highest mass haloes studied here, our measurements are within the finite bin width error, and therefore our results would be consistent with the interpretation that this prescription statistically accounts for secondary spin bias at these masses.

The bottom-left panel of Figure 6 shows the signal that is measured when high and low λ subsamples are fit for both D_t and $(c/a)_{halo}$. This panel demonstrates that this statistical correction only partially accounts for the relative bias. In the low-mass regime, the relative bias is reduced to about half of its original value. In the high-mass regime, a substantial portion of the low λ under-clustering is accounted for, while the high λ over-clustering remains largely unaffected. That is again with the exception of the highest mass bin.

The bottom-middle panel of Figure 6 shows the secondary bias when λ is a function of both $\langle M \rangle$ and D_t . This panel does not show a statistically significant secondary bias. Thus it seems to be the case that spin secondary bias can be accounted for by the mass accretion rate onto haloes and distance to a twin halo. That is, haloes that are found at similar D_t with similar mass accretion rates do not exhibit secondary spin bias. While some of the points are still greater than the finite bin width error, our fits of spin as a function of twin distance and mass accretion rate have some associated error which is not included here. Since all of these properties are correlated with one another, it is difficult and potentially misleading to identify one of age, concentration, sphericity, or mass accretion as being solely responsible for secondary spin bias beyond the contribution of D_t .

7 CONCLUSION

We used haloes from three high resolution N-body simulations spanning from $10^{9.8}$ to $10^{14} h^{-1} M_\odot$ in virial mass. In section 3, we measured the strength of halo spin secondary bias in all three of these simulations. Our measurements demonstrated that the measured relative bias in each mass bin is consistent across all three simulations. This suggests that the signal associated with halo spin secondary bias is independent of the cosmological parameters of the simulation. We now summarize the primary results of our work here.

- We confirmed the finding of [Sato-Polito et al. \(2018\)](#) that for haloes with virial masses of $M_h \lesssim 10^{11.5} h^{-1} M_\odot$, the secondary spin bias signal inverts.

- In section 4, we presented measurements of the local anisotropy surrounding haloes in both Vishnu and ConsueloHD. We found that it does not correlate with halo spin, and thus the [Lacerna & Padilla \(2012\)](#) explanation for secondary spin bias is not supported.

- In section 5, we noted strong inverse correlations between spin and each of halo age, concentration, and sphericity, implying that high spin haloes tend to be young, non-concentrated, and obliquely shaped. Previous studies have found evidence suggesting that secondary spin bias has different causal mechanisms than that of age and concentration ([Gao & White 2007](#); [Faltenbacher & White 2010](#); [Lacerna & Padilla 2012](#); [Salcedo et al. 2018](#)). These anticorrelations suggest that the old and highly concentrated haloes which exhibit strong clustering are a different sample than the high spin haloes which also exhibit strong clustering. That is, these secondary biases are produced by two unique populations, which confirms the previous studies' interpretations.

- All of the properties studied in section 5 correlate with the redshift of the last major merger and show similar secondary bias behavior which is likely driven by neighbour bias ([Salcedo et al. 2018](#)). While it has been noted before that halo spin tends to increase in a merger event ([Maller et al. 2002](#); [Vitvitska et al. 2002](#); [Drakos et al. 2018a,b](#)), this effect extends over the entire redshift range we have probed. This suggests that the lack of a major merger for a long time is just as important in determining a halo's spin.

- We calculated the dimensionless distance D_t to neighbouring haloes of comparable mass ($M_h \leq M_n \leq 3M_h$), and found a slight, yet statistically significant anticorrelation between the halo spin λ and D_t . The slope of this correlation is larger for higher mass haloes. This suggests that high spin haloes are statistically more likely to be found near a neighbouring halo of comparable mass - a *twin*. This relationship introduces a selection effect which we refer to as *twin bias*, whereby high spin haloes are slightly more likely to be found near a twin halo. This selection effect is such

that in the $10^{13 \pm 0.1} h^{-1} M_\odot$ mass regime, splitting haloes into the top and bottom 50% spin samples results in the high spin sample containing $\sim 15\%$ more $D_t \lesssim 10$ haloes than the low spin sample. Furthermore, the quantity D_t exhibits a strong spatial bias, which is unsurprising since low D_t haloes are by definition near another halo of comparable mass.

- While the λ - D_t relation is weak, we demonstrated that when high and low spin samples are drawn from a high-order polynomial fit to λ as a function of D_t , a large portion of the secondary bias signal is removed. The only statistically significant signal that remained was below the turnover at $10^{11.5} h^{-1} M_\odot$. This suggests that twin bias plays a key role in producing the spin dependence of halo clustering. Furthermore, we also saw that when we account for twin bias along with halo age or concentration, a mild, mass-independent secondary bias is produced. When we account for twin bias in combination with halo sphericity, the relative bias is reduced but a significant signal remains. In the case of mass accretion rate, it nearly disappears entirely, with outliers in only a few mass bins. That is, haloes with similar mass accretion rates found at similar distances to comparable mass neighbours do not exhibit secondary spin bias. However, because all of these properties are related to one another, it is difficult and potentially misleading to identify one of age, concentration, sphericity, or mass accretion as the primary driver of this residual signal. We therefore conclude that secondary spin bias is a two-term phenomenon, where the signal is largely driven by twin bias, but is also influenced by the correlation between spin and other halo properties which also exhibit secondary biases.

[Salcedo et al. \(2018\)](#) showed that the same formulation of distance applied to more massive neighbours ($M_n \geq 10M_h$) does not show a correlation with spin. Twin bias only applies to neighbouring haloes of comparable mass, and for this reason it is fundamentally different from neighbour bias. When a halo is near a much more massive neighbour ($M_n \gtrsim 3M_h$), this causes arrested development, which prevents high angular momentum material from accreting onto the halo. When the neighbour has less mass ($M_n \sim M_h$), the twin tidally torques the halo, but does not affect accretion since it is not heavy enough to cause arrested development.

There are a couple possible interpretations of the relationship between λ and D_t that we note here. First, it could be that the probability of a halo having a twin correlates with the large scale tidal field. Second, simply the presence of the twin may produce a tidal torque. The first interpretation, but not the second, would explain why the correlation between λ and D_t appears to continue at large D_t . However, these interpretations are not mutually exclusive, and further studies will be required to explore the full details of twin bias.

8 ACKNOWLEDGEMENTS

J.W.J. would like to thank Robert Scherrer and Jonathan Bird at Vanderbilt University for participating in a review committee with J.K.H-B. and A.A.B. when this project was at the undergraduate thesis level. Some of the computation for this work was done using the Advanced Computing Center for Research and Education (ACCRE) at Vanderbilt University. J.W.J. also acknowledges the valuable comments on this work contributed by David H. Weinberg and Andres N. Salcedo at The Ohio State University. A.A.B. was supported by the National Science Foundation (NSF) through a Career Award (AST-1151650). This work used the Extreme Science and Engineering Discovery Environment (XSEDE) ([Towns et al.](#)

2014), which is supported by National Science Foundation grant number ACI-1548562, through allocations TG-AST080002N and TG-AST130037. MS would like to thank Matt Becker for sharing the memory-efficient `uber-LGadget2` that was used to run the `ConsueloHD` and `Vishnu` simulations. Parts of this research were conducted by the Australian Research Council Centre of Excellence for All Sky Astrophysics in 3 Dimensions (ASTRO 3D), through project number CE170100013. The authors gratefully acknowledge the Gauss Centre for Supercomputing e.V. (www.gauss-centre.eu) and the Partnership for Advanced Supercomputing in Europe (PRACE, www.prace-ri.eu) for funding the `MultiDark` simulation project by providing computing time on the GCS Supercomputer SuperMUC at Leibniz Supercomputing Centre (LRZ, www.lrz.de).

REFERENCES

- Behroozi P. S., Wechsler R. H., Wu H.-Y., 2013a, *ApJ*, **762**, 109
- Behroozi P. S., Wechsler R. H., Wu H.-Y., Busha M. T., Klypin A. A., Primack J. R., 2013b, *ApJ*, **763**, 18
- Benson A. J., 2017, *MNRAS*, **471**, 2871
- Berlind A. A., Weinberg D. H., 2002, *ApJ*, **575**, 587
- Berlind A. A., et al., 2003, *ApJ*, **593**, 1
- Brook C. B., et al., 2011, *MNRAS*, **415**, 1051
- Brook C. B., Stinson G., Gibson B. K., Roškar R., Wadsley J., Quinn T., 2012, *MNRAS*, **419**, 771
- Bryan G. L., Norman M. L., 1998, *ApJ*, **495**, 80
- Bullock J. S., Dekel A., Kolatt T. S., Kravtsov A. V., Klypin A. A., Porciani C., Primack J. R., 2001, *ApJ*, **555**, 240
- Conroy C., Wechsler R. H., Kravtsov A. V., 2006, *ApJ*, **647**, 201
- Cooray A., Sheth R., 2002, *Phys. Rep.*, **372**, 1
- Croton D. J., Gao L., White S. D. M., 2007, *MNRAS*, **374**, 1303
- Drakos N. E., Taylor J. E., Berrouet A., Robotham A. S. G., Power C., 2018a, preprint, ([arXiv:1811.12839](https://arxiv.org/abs/1811.12839))
- Drakos N. E., Taylor J. E., Berrouet A., Robotham A. S. G., Power C., 2018b, preprint, ([arXiv:1811.12844](https://arxiv.org/abs/1811.12844))
- Fall S. M., Efstathiou G., 1980, *MNRAS*, **193**, 189
- Faltenbacher A., White S. D. M., 2010, *ApJ*, **708**, 469
- Gao L., White S. D. M., 2007, *MNRAS*, **377**, L5
- Gao L., Springel V., White S. D. M., 2005, *MNRAS*, **363**, L66
- Hearin A. P., Watson D. F., 2013, *MNRAS*, **435**, 1313
- Hearin A. P., Watson D. F., Becker M. R., Reyes R., Berlind A. A., Zentner A. R., 2014, *MNRAS*, **444**, 729
- Hearin A. P., Watson D. F., van den Bosch F. C., 2015, *MNRAS*, **452**, 1958
- Klypin A. A., Trujillo-Gomez S., Primack J., 2011, *ApJ*, **740**, 102
- Klypin A., Yepes G., Gottlöber S., Prada F., Heß S., 2016, *MNRAS*, **457**, 4340
- Lacerna I., Padilla N., 2012, *MNRAS*, **426**, L26
- Landy S. D., Szalay A. S., 1993, *ApJ*, **412**, 64
- Lazeyras T., Musso M., Schmidt F., 2017, *J. Cosmology Astropart. Phys.*, **3**, 059
- Lewis A., Challinor A., 2011, *CAMB: Code for Anisotropies in the Microwave Background*, Astrophysics Source Code Library ([ascl:1102.026](https://arxiv.org/abs/1102.026))
- Li Y., Mo H. J., Gao L., 2008, *MNRAS*, **389**, 1419
- Maller A. H., Dekel A., 2002, *MNRAS*, **335**, 487
- Maller A. H., Dekel A., Somerville R., 2002, *MNRAS*, **329**, 423
- Mao Y.-Y., Zentner A. R., Wechsler R. H., 2018, *MNRAS*, **474**, 5143
- Mo H. J., White S. D. M., 1996, *MNRAS*, **282**, 347
- Mo H. J., Mao S., White S. D. M., 1998, *MNRAS*, **295**, 319
- Navarro J. F., Frenk C. S., White S. D. M., 1997, *ApJ*, **490**, 493
- Oñorbe J., Garrison-Kimmel S., Maller A. H., Bullock J. S., Rocha M., Hahn O., 2014, *MNRAS*, **437**, 1894
- Peacock J. A., Smith R. E., 2000, *MNRAS*, **318**, 1144
- Peebles P. J. E., 1969, *ApJ*, **155**, 393
- Prada F., Klypin A. A., Cuesta A. J., Betancort-Rijo J. E., Primack J., 2012, *MNRAS*, **423**, 3018
- Press W. H., Schechter P., 1974, *ApJ*, **187**, 425
- Salcedo A. N., Maller A. H., Berlind A. A., Sinha M., McBride C. K., Behroozi P. S., Wechsler R. H., Weinberg D. H., 2018, *MNRAS*, **475**, 4411
- Sato-Polito G., Montero-Dorta A. D., Abramo L. R., Prada F., Klypin A., 2018, preprint, ([arXiv:1810.02375](https://arxiv.org/abs/1810.02375))
- Schneider M. D., Frenk C. S., Cole S., 2012, *J. Cosmology Astropart. Phys.*, **5**, 030
- Scoccimarro R., 1997, *ApJ*, **487**, 1
- Scoccimarro R., Sheth R. K., Hui L., Jain B., 2001, *ApJ*, **546**, 20
- Sheth R. K., Tormen G., 2004, *MNRAS*, **350**, 1385
- Somerville R. S., et al., 2008, *ApJ*, **672**, 776
- Somerville R. S., et al., 2018, *MNRAS*, **473**, 2714
- Springel V., 2005, *MNRAS*, **364**, 1105
- Towns J., et al., 2014, *Computing in Science & Engineering*, **16**, 62
- Vale A., Ostriker J. P., 2004, *MNRAS*, **353**, 189
- Villarreal A. S., et al., 2017, *MNRAS*, **472**, 1088
- Vitvitska M., Klypin A. A., Kravtsov A. V., Wechsler R. H., Primack J. R., Bullock J. S., 2002, *ApJ*, **581**, 799
- Wang H. Y., Mo H. J., Jing Y. P., 2007, *MNRAS*, **375**, 633
- Wechsler R. H., Zentner A. R., Bullock J. S., Kravtsov A. V., Allgood B., 2006, *ApJ*, **652**, 71
- Yang X., Mo H. J., van den Bosch F. C., 2003, *MNRAS*, **339**, 1057
- Zu Y., Mandelbaum R., 2015, *MNRAS*, **454**, 1161
- Zu Y., Mandelbaum R., 2016, *MNRAS*, **457**, 4360
- van den Bosch F. C., Yang X., Mo H. J., 2003, *MNRAS*, **340**, 771

This paper has been typeset from a $\text{\TeX}/\text{\LaTeX}$ file prepared by the author.